

J-PLUS: Systematic impact of metallicity on photometric calibration with the stellar locus

C. López-Sanjuan¹, H. Yuan², H. Vázquez Ramió¹, J. Varela¹, D. Cristóbal-Hornillos³, P. -E. Tremblay⁴,
A. Marín-Franch¹, A. J. Cenarro¹, A. Ederoclite⁵, E. J. Alfaro⁶, A. Alvarez-Candal^{6,7,8}, S. Daflon⁸,
A. Hernán-Caballero³, C. Hernández-Monteagudo^{9,10,1}, F. M. Jiménez-Esteban^{11,12}, V. M. Placco¹³, E. Tempel¹⁴,
J. Alcaniz⁸, R. E. Angulo^{15,16}, R. A. Dupke^{8,17,18}, M. Moles³, and L. Sodr e Jr.⁵

¹ Centro de Estudios de Física del Cosmos de Aragón (CEFCA), Unidad Asociada al CSIC, Plaza San Juan 1, 44001 Teruel, Spain
e-mail: c1sj@cefca.es

² Department of Astronomy, Beijing Normal University, Beijing 100875, People's Republic of China

³ Centro de Estudios de Física del Cosmos de Aragón (CEFCA), Plaza San Juan 1, 44001 Teruel, Spain

⁴ Department of Physics, University of Warwick, Coventry, CV4 7AL, UK

⁵ Instituto de Astronomia, Geofísica e Ciências Atmosféricas, Universidade de São Paulo, 05508-090 São Paulo, Brazil

⁶ Instituto de Astrofísica de Andalucía (IAA-CSIC), Glorieta de la astronomía s/n, 18008 Granada, Spain

⁷ IUFACyT, Universidad de Alicante, San Vicent del Raspeig, 03080 Alicante, Spain

⁸ Observatório Nacional, Rua General José Cristino, 77 - Bairro Imperial de São Cristóvão, 20921-400 Rio de Janeiro, Brazil

⁹ Instituto de Astrofísica de Canarias (IAC), 38205 La Laguna, Spain

¹⁰ Departamento de Astrofísica, Universidad de La Laguna (ULL), 38200 La Laguna, Spain

¹¹ Centro de Astrobiología (CSIC-INTA), ESAC Campus, Camino Bajo del Castillo s/n, 28692 Villanueva de la Cañada, Spain

¹² Spanish Virtual Observatory, 28692 Villanueva de la Cañada, Spain

¹³ Community Science and Data Center/NSF's NOIRLab, 950 N. Cherry Ave., Tucson, AZ 85719, USA

¹⁴ Tartu Observatory, University of Tartu, Observatooriumi 1, 61602 Tõravere, Estonia

¹⁵ Donostia International Physics Centre (DIPC), Paseo Manuel de Lardizabal 4, 20018 Donostia-San Sebastián, Spain

¹⁶ IKERBASQUE, Basque Foundation for Science, 48013, Bilbao, Spain

¹⁷ University of Michigan, Department of Astronomy, 1085 South University Ave., Ann Arbor, MI 48109, USA

¹⁸ University of Alabama, Department of Physics and Astronomy, Gallalee Hall, Tuscaloosa, AL 35401, USA

Received 29 January 2021

ABSTRACT

Aims. We present the updated photometric calibration of the twelve optical passbands for the Javalambre Photometric Local Universe Survey (J-PLUS) second data release (DR2), comprising 1 088 pointings of two square degrees, and study the systematic impact of metallicity in the stellar locus technique.

Methods. The [Fe/H] metallicity from LAMOST DR5 for 146 184 high-quality calibration stars, defined with S/N > 10 in J-PLUS passbands and S/N > 3 in *Gaia* parallax, was used to define the metallicity-dependent stellar locus (ZSL). The initial homogenization of J-PLUS photometry, performed with a unique stellar locus, was refined by including the metallicity effect in colours via the ZSL.

Results. The variation of the average metallicity along the Milky Way produces a systematic offset in J-PLUS calibration. This effect is well above 1% for the bluer passbands and amounts 0.07, 0.07, 0.05, 0.03, and 0.02 mag in *u*, *J0378*, *J0395*, *J0410*, and *J0430*, respectively. We modelled this effect with the Milky Way location of the J-PLUS pointing, providing also an updated calibration for those observations without LAMOST information. The estimated accuracy in the calibration after including the metallicity effect is at 1% level for the bluer J-PLUS passbands and below for the rest.

Conclusions. Photometric calibration with the stellar locus technique is prone to significant systematic bias along the Milky Way location for passbands bluer than $\lambda = 4\,500\text{ \AA}$. The updated calibration method for J-PLUS DR2 reaches 1-2% precision and 1% accuracy for twelve optical filters within an area of 2 176 square degrees.

Key words. methods:statistical, techniques:photometric, surveys

1. Introduction

One fundamental step in the data processing of any imaging survey is the photometric calibration of the observations. The calibration process aims to translate the observed counts in astronomical images to a physical flux scale referred to the top of the atmosphere. Because accurate colours are needed to derive photometric redshifts for galaxies, atmospheric parameters for Milky Way (MW) stars, and surface characteristics for minor bodies; and reliable absolute fluxes are involved in the estima-

tion of the luminosity and the stellar mass of galaxies, current and future photometric surveys target a calibration uncertainty at the 1% level and below to reach their ambitious scientific goals.

One particular approach to perform the photometric calibration is the use of the stellar locus (Covey et al. 2007; High et al. 2009; Kelly et al. 2014). This procedure takes advantage of the way stars with different stellar parameters populate colour-colour diagrams, defining a well-constrained region (stellar locus) whose shape depends on the specific colours used. The

Table 1. J-PLUS photometric system, extinction coefficients, and limiting magnitudes (5σ , $3''$ aperture) of J-PLUS DR2.

Passband (λ)	Central Wavelength [nm]	FWHM [nm]	$m_{\text{lim}}^{\text{DR2}}$ [AB]	$k_X = \frac{A_X}{E(B-V)}$	Comments
<i>u</i>	348.5	50.8	20.8	4.479	In common with J-PAS
J0378	378.5	16.8	20.8	4.294	[OII]; in common with J-PAS
J0395	395.0	10.0	20.8	4.226	Ca H+K; similar to the CaHK filter from <i>Pristine</i>
J0410	410.0	20.0	21.0	4.023	H δ
J0430	430.0	20.0	21.0	3.859	G band
<i>g</i>	480.3	140.9	21.8	3.398	SDSS
J0515	515.0	20.0	21.0	3.148	Mgb Triplet
<i>r</i>	625.4	138.8	21.8	2.383	SDSS
J0660	660.0	13.8	21.0	2.161	H α ; in common with J-PAS
<i>i</i>	766.8	153.5	21.3	1.743	SDSS
J0861	861.0	40.0	20.4	1.381	Ca Triplet
<i>z</i>	911.4	140.9	20.5	1.289	SDSS

match between the instrumental data and a reference stellar locus provides the flux calibration of the images.

The stellar locus technique is able to provide a photometric calibration without the need of dedicated calibration images of standard stars, saving telescope time and optimizing operations. Its main assumption is that the reference locus is valid for any observed position. In the general case, the stellar photometry in the Galaxy is affected by the amount of interstellar matter that star-light passes through until reaching the observer and by possible local variations in the extinction law. This leaves two solutions to define the reference locus: de-reddening the photometry, which implies knowing (or assuming) in each case the local extinction law, or choosing a set of dust-free objects. It would be a way of saying that we need photometry "outside" the Galaxy to set the stellar locus as reference (High et al. 2009).

In addition to the interstellar extinction, the average properties of the stars also varies with their position in the MW. The stellar locus location for main sequence (MS) stars is dominated by temperature variations, so the measured correlation in colour-colour diagrams is roughly a temperature sequence. However, the metallicity is also a relevant parameter that affects appreciably the stellar locus location (e.g. Lenz et al. 1998; Ivezić et al. 2008; Yuan et al. 2015a; Kesseli et al. 2017), specially at the bluer optical passbands. With the average metallicity of the observed MW stars decreasing as we move from disk-dominated ($[\text{Fe}/\text{H}] \sim -0.5$ dex) to halo-dominated ($[\text{Fe}/\text{H}] \sim -1.5$ dex) sky positions (Ivezić et al. 2008), the location of the stellar locus changes accordingly and the assumption of a position-independent reference locus is not valid. This metallicity effect shall be the leading source of systematic in the calibration with the stellar locus technique.

Several large-area photometric surveys covering the blue edge ($\lambda < 4500$ Å) of the optical range rely on the stellar locus technique for calibration. We highlight the Kilo-Degree Survey (KiDS, Kuijken et al. 2019; *ugriz* broad bands), the *Pristine* survey (Starkenburg et al. 2017; a unique CaHK filter of 98 Å width centered at 3952 Å), and the Javalambre Photometric Local Universe Survey (J-PLUS, Cenarro et al. 2019; 5 broad + 7 medium optical filters as summarised in Table 1). There are hints in these surveys about the impact of metallicity variations in the stellar locus calibration. For example, the comparison of the KiDS *u* band with the Sloan Digital Sky Survey (SDSS, Aihara et al. 2011) photometry reveals a systematic variation with galactic latitude, that the authors link to the change in metallicity (Kuijken et al. 2019). Furthermore, the photometric metallicity

derived from *Pristine* presents a systematic variation with the sky position when the stellar locus calibration is performed with $0.4 < (g - i) < 1.2$ stars. They conclude that this is a reflection of the metallicity impact in the stellar locus, and proper measurements are reached by calibrating with dwarf MS stars in the range $1.2 < (g - i) < 2.4$ (Starkenburg et al. 2017).

The J-PLUS second data release (DR2; Varela & J-PLUS collaboration 2021), covering 2 176 deg², was made public in November 2020, and we describe here its photometric calibration. It is based on the stellar and white dwarf loci procedure detailed in López-Sanjuan et al. (2019) and that was applied to J-PLUS first data release (DR1). In the present paper, we took advantage of the $[\text{Fe}/\text{H}]$ information provided by the Large Sky Area Multi-Object Fibre Spectroscopic Telescope (LAMOST, Cui et al. 2012) surveys to implement the metallicity-dependent stellar locus for calibration. That improved the accuracy of the J-PLUS DR2 photometry, specially at passbands bluer than $\lambda = 4500$ Å, and highlights the systematic variation of the photometric solution with the position in the sky when metallicity effects are neglected.

In addition to a metallicity-dependent stellar locus, the access to massive spectroscopic information also permits the application of the Stellar Color Regression (SCR, Yuan et al. 2015b; Huang et al. 2020) method. Using T_{eff} , $\log g$, and $[\text{Fe}/\text{H}]$ from spectroscopy, the SCR matches stars of the same properties, i.e. intrinsic colours, and assigns observed colour differences to the effect of interstellar extinction. This permits to homogenize the photometric solution by naturally accounting for temperature, gravity, and metallicity effects. The application of the SCR to J-PLUS data is beyond the scope of the present paper, and it is explored in a forthcoming work.

This paper is organized as follows. The J-PLUS DR2 and the ancillary data used on its calibration are presented in Sect. 2. The calibration methodology is summarised in Sect. 3, highlighting the addition of the metallicity-dependent stellar locus in the process. The precision, accuracy, and the systematic impact of metallicity in the J-PLUS DR2 calibration are discussed in Sect. 4. We devoted Sect. 5 to summarise the work and present our conclusions. Magnitudes are given in the AB system (Oke & Gunn 1983).

2. J-PLUS photometric data

J-PLUS¹ is being conducted from the Observatorio Astrofísico de Javalambre (OAJ, Teruel, Spain; Cenarro et al. 2014) using the 83 cm Javalambre Auxiliary Survey Telescope (JAST/T80) and T80Cam, a panoramic camera of $9.2k \times 9.2k$ pixels that provides a 2 deg^2 field of view (FoV) with a pixel scale of $0.55'' \text{ pix}^{-1}$ (Marín-Franch et al. 2015). The J-PLUS filter system, composed of twelve bands, is summarized in Table 1. These filters were designed to optimise the characterization of MW stars. The J-PLUS observational strategy, image reduction, and main scientific goals are presented in Cenarro et al. (2019). In addition to its scientific potential, J-PLUS was defined with the technical goal of ensure the photometric calibration of the Javalambre Physics of the Accelerating Universe Astrophysical Survey (J-PAS; Benítez et al. 2014; Bonoli et al. 2020), that will scan thousands of square degrees with 56 narrow bands of $\sim 140 \text{ \AA}$ width down to $m \sim 22.5$ mag from the OAJ.

The J-PLUS DR2 comprises 1 088 pointings ($2 176 \text{ deg}^2$) observed and reduced in all survey bands (Varela & J-PLUS collaboration 2021). The limiting magnitudes (5σ , $3''$ aperture) of the DR2 are presented in Table 1 for reference. The median point spread function (PSF) full width at half maximum (FWHM) in the DR2 r -band images is $1.1''$. Source detection was done in the r band using SExtractor (Bertin & Arnouts 1996), and the flux measurement in the twelve J-PLUS bands was performed at the position of the detected sources using the aperture defined in the r -band image. Objects near the borders of the images, close to bright stars, or affected by optical artefacts were masked. The DR2 is publicly available at the J-PLUS website².

The calibration process presented in Sect. 3 uses J-PLUS DR2 in combination with ancillary data from *Gaia*, the Panoramic Survey Telescope and Rapid Response System (Pan-STARRS), and LAMOST. We describe these datasets in the following.

2.1. Pan-STARRS DR1

The Pan-STARRS1 is a 1.8 m optical and near-infrared telescope located on Mount Haleakala, Hawaii. The telescope is equipped with the Gigapixel Camera 1 (GPC1), consisting of an array of 60 CCD detectors, each 4 800 pixels by side (Chambers et al. 2016).

The 3π Steradian Survey (hereafter PS1; Chambers et al. 2016) covers the sky north of declination $\delta = -30^\circ$ in four SDSS-like passbands, *griz*, with an additional passband in the near-infrared, *y*. The entire filter set spans the range 400 – 1 000 nm (Tonry et al. 2012).

Astrometry and photometry were extracted by the Pan-STARRS1 Image Processing Pipeline (Magnier et al. 2016a,b,c; Waters et al. 2016). PS1 photometry features a uniform flux calibration, achieving better than 1% precision over the sky (Magnier et al. 2016b; Chambers et al. 2016). In single-epoch photometry, PS1 reaches typical 5σ depths of 22.0, 21.8, 21.5, 20.9, and 19.7 in *grizy*, respectively (Chambers et al. 2016). The PS1 DR1 occurred in December 2016, and provided a static-sky catalogue, stacked images from the 3π Steradian Survey, and other data products (Flewelling et al. 2016).

Because of its large footprint, homogeneous depth, and excellent internal calibration, PS1 photometry provides an ideal reference for the calibration of the *gri* J-PLUS broad bands. The

z -band photometry from PS1 was reserved to test the calibration procedure.

2.2. Gaia DR2

The *Gaia* spacecraft is mapping the 3D positions and kinematics of a representative fraction of MW stars (Gaia Collaboration et al. 2016). The mission will eventually provide astrometry (positions, proper motions, and parallaxes) and optical spectrophotometry for over a billion stars, as well as radial velocity measurements of more than 100 million stars.

In the present paper, we used the *Gaia* DR2 (Gaia Collaboration et al. 2018), that is based on 22 months of observations. It contains five-parameter astrometric determinations and provides integrated photometry in three broad bands, G (330 – 1 050 nm), G_{BP} (330 – 680 nm), and G_{RP} (630 – 1 050 nm), for 1.4 billion sources with $G < 21$. The typical uncertainties in *Gaia* DR2 measurements at $G = 17$ are ~ 0.1 marcsec in parallax, ~ 2 mmag in G -band photometry, and ~ 10 mmag in G_{BP} and G_{RP} magnitudes (Gaia Collaboration et al. 2018).

2.3. LAMOST DR5

LAMOST is a 4-metre quasi-meridian reflecting Schmidt telescope equipped with thousands of fibers distributed in a FoV of about 20 deg^2 . It can simultaneously collect spectra per exposure of up to 4 000 objects, covering the wavelength range 380 – 900 nm at a resolving power of $R \sim 1 800$ (Cui et al. 2012). The five-year Phase I LAMOST regular surveys started in the fall of 2012 and were completed in the summer of 2017. The scientific motivations and target selections of these surveys are described in Zhao et al. (2012); Deng et al. (2012); Luo et al. (2015); and Yuan et al. (2015c).

On the final data release of the LAMOST Phase I surveys, the LAMOST DR5 provides to the community 9 027 634 optical spectra, of which more than 90 percent are stellar. The LAMOST DR5 provides stellar classifications and radial velocity measurements for these spectra. We restricted in the present work to the 5 348 712 objects in the *A*, *F*, *G*, and *K* type star catalog³, that includes the basic stellar parameters T_{eff} , $\log g$, and $[\text{Fe}/\text{H}]$ derived with the LAMOST stellar parameter pipeline (LASP; Wu et al. 2011; Luo et al. 2015).

3. Photometric calibration of J-PLUS DR2

The photometric calibration of the J-PLUS DR2 data follows the main steps presented in López-Sanjuan et al. (2019) for the calibration of J-PLUS DR1. We provide a brief summary of the process in Sect. 3.1. The main improvement with respect to DR1 procedure is the inclusion of the metallicity effect in the stellar locus location, as detailed in Sect. 3.2.

The goal of any calibration strategy is to obtain the zero point (ZP) of the observation, that relates the magnitude of the sources in passband X on top of the atmosphere with the magnitudes obtained from the analogue to digital unit (ADU) counts of the reduced images. We simplify the notation in the following using the passband name as the magnitude in such filter. Thus,

$$X = -2.5 \log_{10}(\text{ADU}_X) + \text{ZP}_X. \quad (1)$$

In the estimation of the J-PLUS DR2 raw catalogues, the reduced images were normalized to a one-second exposure and an arbi-

¹ www.j-plus.es

² www.j-plus.es/datareleases/data_release_dr2

³ http://dr5.lamost.org/v3/doc/data-production-description#toc_16

trary instrumental zero point $ZP_{\mathcal{X}} = 25$ was set. This defined the instrumental magnitudes \mathcal{X}_{ins} .

The calibration process applied in J-PLUS DR2 have different steps, as described in Sect. 3.1. At the end, we estimated the zero point of the passband \mathcal{X} in the pointing p_{id} as

$$ZP_{\mathcal{X}}(p_{\text{id}}, \mathcal{X}, Y) = \Delta\mathcal{X}_{\text{atm}}(p_{\text{id}}) + P_{\mathcal{X}}(p_{\text{id}}, \mathcal{X}, Y) + \Delta\mathcal{X}_{\text{FeH}}(p_{\text{id}}) + \Delta\mathcal{X}_{\text{WD}} + 25, \quad (2)$$

where $\Delta\mathcal{X}_{\text{atm}}$ is the term that accounts for the atmospheric extinction at the moment of the observation, $P_{\mathcal{X}}$ defines a plane that accounts for the 2D variation of the calibration with the (X, Y) position of the sources on the CCD, $\Delta\mathcal{X}_{\text{FeH}}$ includes the effect of the metallicity in the stellar locus homogenization process, and $\Delta\mathcal{X}_{\text{WD}}$ is the global offset provided by the white dwarf (WD) locus that translates homogenized magnitudes to calibrated magnitudes outside the atmosphere.

The J-PLUS instrumental magnitudes used for calibration were measured on a $6''$ diameter aperture. This aperture is not dominated by background noise and limits the flux contamination from neighbouring sources, although it is not large enough to capture the total flux of the stars. Thus, we applied an aperture correction C_{aper} that depends on the pointing and the passband. The aperture correction was computed from the growth curves of bright, non-saturated stars in the pointing. For each star, increasingly larger circular apertures were measured until convergence within errors. This defined the aperture size that provides the total magnitude of the sources in the pointing, that is then compared with the magnitude at $6''$ aperture to provide C_{aper} . The typical number of stars used is 50 and the median aperture correction varies from $C_{\text{aper}} = -0.09$ mag in the u band to $C_{\text{aper}} = -0.11$ mag in the z band, with a median value of $C_{\text{aper}} = -0.09$ mag for all the filters. The typical uncertainty in the correction aperture, estimated from the dispersion in the measurements, is ~ 2 mmag. We assumed that the J-PLUS $6''$ magnitudes corrected for aperture effects provided the total flux of stars.

We worked with dust de-reddened magnitudes and colours in several stages of the calibration process. We empirically computed the extinction coefficients $k_{\mathcal{X}}$ of each J-PLUS passband, presented in Table 1, by applying the star-pair technique described in Yuan et al. (2013) to J-PLUS DR1. The de-reddened J-PLUS photometry, either instrumental or calibrated, is noted with the subscript 0 and was obtained as

$$\mathcal{X}_0 = \mathcal{X} - k_{\mathcal{X}}E(B - V). \quad (3)$$

We estimated the colour excess at infinite distance of each J-PLUS source from the Schlegel et al. (1998) extinction map. The stars used in the calibration process have distance information from *Gaia* DR2 parallaxes (Sect. 3.1), and we included the 3D information using the MW dust model presented in Li et al. (2018). We integrated the dust model to infinity and to the distance provided by *Gaia* at star location, scaling accordingly the colour excess from Schlegel et al. (1998) map to obtain $E(B - V)$. The uncertainty in $E(B - V)$ was fixed to 0.012 mag. This error was estimated by comparing the colour excess directly measured from the star-pair method (Yuan et al. 2013) with the assumed $E(B - V)$. The dispersion in this comparison was set as the uncertainty in the used 3D extinction. We test the assumed extinction correction in Sect. 4.3.

3.1. Scheme of the calibration process

We provide in this section a brief summary of the steps involved in the photometric calibration of J-PLUS DR2 images. The up-

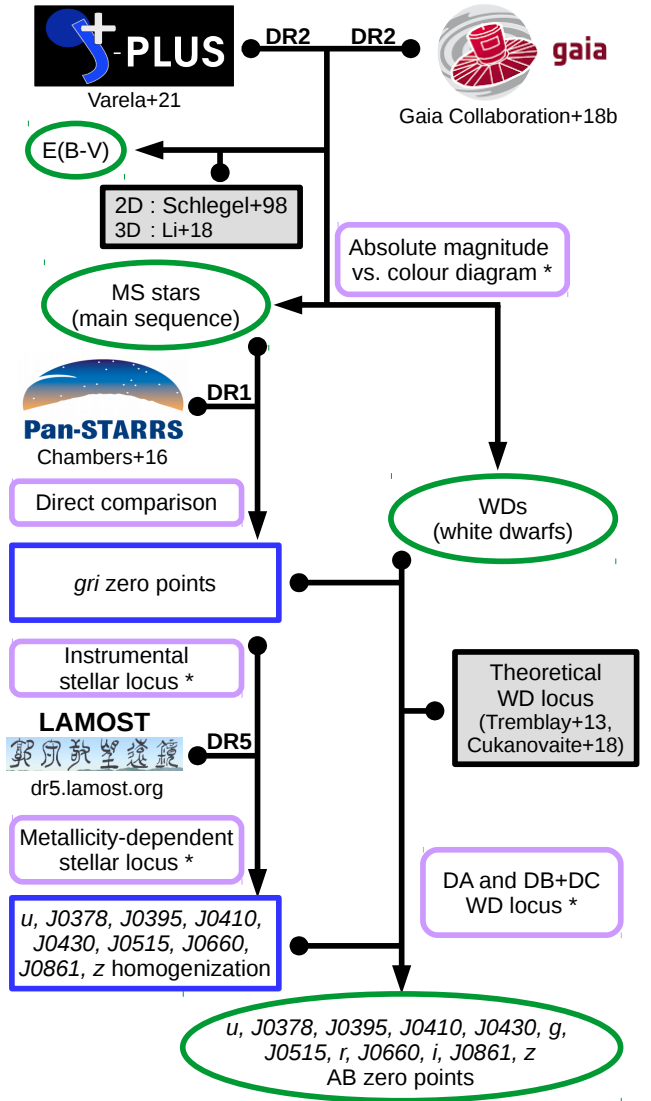


Fig. 1. Updated flowchart of the calibration method used in this work. Arrows that originate in small dots indicate that the preceding data product is an input to the subsequent analysis. Datasets are shown with their project logo, and external codes or models with grey boxes. The rounded-shape boxes show the calibration steps. The asterisks indicate those steps based on dust de-reddened magnitudes. The white boxes show intermediate data products, and ovals highlight data products of the calibration process. The changes with respect to J-PLUS DR1 calibration are the modification in the assumed dust extinction and the addition of the metallicity-dependent stellar locus step in the homogenization (Sect. 3.2).

dated flowchart of the calibration process is presented in Fig. 1. We refer the reader to López-Sanjuan et al. (2019) for an extensive description of the calibration procedure but the metallicity-dependent stellar locus step, added for J-PLUS DR2 and described in Sect. 3.2. The calibration steps were:

- Definition of a high-quality sample of MS stars for calibration. We selected those sources in common between J-PLUS DR2 and *Gaia* DR2 with signal-to-noise (S/N) larger than ten in all the photometric bands and with $S/N > 3$ in *Gaia* parallax. We constructed the dust de-reddened absolute G magnitude versus $G_{\text{BP}} - G_{\text{RP}}$ diagram and selected those sources belonging to the main sequence. This provided

1 117 073 MS calibration stars, with a median of 822 calibration stars per pointing and a minimum of 92 stars.

- Calibration of the *gri* broad-band filters with PS1 photometry. The J-PLUS instrumental magnitudes were compared with the PSF magnitudes in PS1 after accounting for the colour terms between both photometric systems. This step provides the $\Delta\mathcal{X}_{\text{atm}}$ and the 2D variation along the CCD of the *gri* broad-band filters. Because we used PS1 calibrated magnitudes as reference, $\Delta\mathcal{X}_{\text{FeH}} = 0$ and $\Delta\mathcal{X}_{\text{WD}} \sim 0$. The latter term is not zero because residual differences between J-PLUS and PS1 photometric systems can exist, as discussed in Sect. 4.3.
- Initial homogenization of the narrow bands with the instrumental stellar locus (ISL). For each remaining passband, we computed the dust de-reddened $(\mathcal{X}_{\text{ins}} - r)_0$ versus $(g - i)_0$ colour-colour diagrams of the MS calibration stars. From these, we computed the offsets that lead to a consistent ISL among all the J-PLUS DR2 pointings. This provides $\Delta\mathcal{X}_{\text{atm}}$ and the 2D variation along the CCD for the other nine J-PLUS passbands. After this step, we defined the ISL magnitudes as

$$\mathcal{X}_{\text{ISL}} = \mathcal{X}_{\text{ins}} + \Delta\mathcal{X}_{\text{atm}} + P_{\mathcal{X}}. \quad (4)$$

- Final homogenization with the metallicity-dependent stellar locus (ZSL). We refined the methodology presented in López-Sanjuan et al. (2019) by including the effect of metallicity in the stellar locus location. We used the metallicity measurements from LAMOST DR5 and the procedure is fully detailed in Sect. 3.2. This step provided $\Delta\mathcal{X}_{\text{FeH}}$, defining the ISL + ZSL magnitudes

$$\mathcal{X}_{\text{ISL+ZSL}} = \mathcal{X}_{\text{ISL}} + \Delta\mathcal{X}_{\text{FeH}}. \quad (5)$$

- Absolute colour calibration with the white dwarf locus. From the *Gaia* absolute magnitude versus colour diagram in the first step, we also selected 639 high-quality WDs. We compared the observed colour-colour locus in $(\mathcal{X}_{\text{ISL+ZSL}} - r)_0$ versus $(g - i)_0$ with the theoretical expectations from pure hydrogen (DA; Tremblay et al. 2013) and pure helium (DB and DC; Cukanovaite et al. 2018) models. The Bayesian modeling of the WD locus provided the $\Delta\mathcal{X}_{\text{WD}}$ for all the passbands but *r*, that was used as the reference band in the process.

The performance of J-PLUS DR2 calibration is presented in Sect. 4. The median zero points obtained after the complete calibration process are presented in Table 2 for reference.

3.2. Implementation of the metallicity-dependent stellar locus

The calibration process presented in López-Sanjuan et al. (2019) and summarised in the previous section was updated for J-PLUS DR2 by including the impact of metallicity in the stellar locus location. We use the *u* band as reference to illustrate the process, and the methodology was similar for other J-PLUS passbands but *gri*, anchored to PS1 photometry. The improvement in the accuracy of J-PLUS calibration along the surveyed area from this step is presented in Sect. 4.2.

3.2.1. LAMOST cross-match with the calibration sample

We started by gathering the $[\text{Fe}/\text{H}]$ (dubbed metallicity hereafter) information of the MS calibration stars. We cross-matched the calibration sample with the LAMOST catalogue using a 1 arcsec radius. A total of 146 184 sources in common were retrieved.

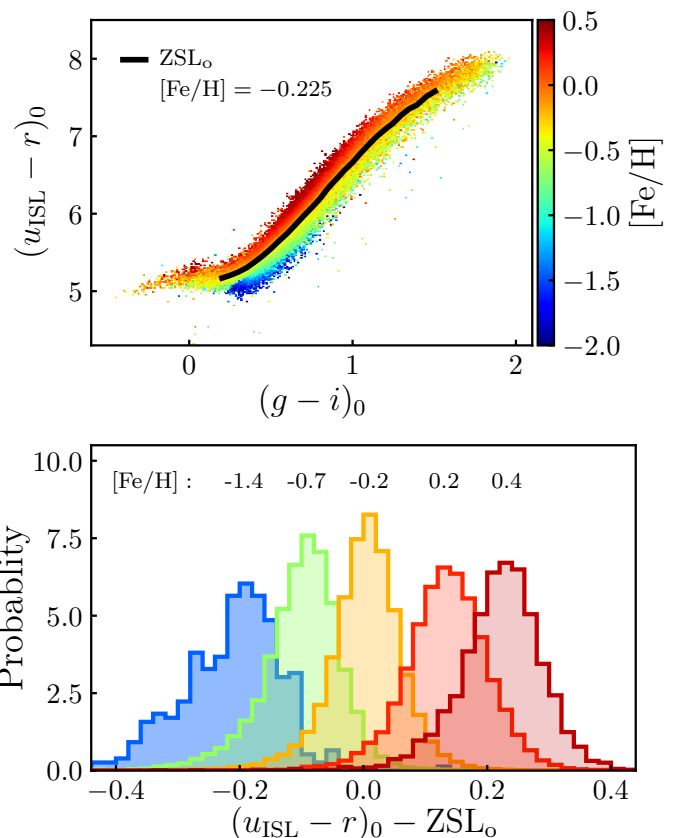


Fig. 2. *Top panel:* Binned $(u_{\text{ISL}} - r)_0$ versus $(g - i)_0$ colour-colour diagram. The colour scale shows the median $[\text{Fe}/\text{H}]$ in each bin estimated from LAMOST spectra. The black solid line marks the stellar locus for $-0.25 < [\text{Fe}/\text{H}] < -0.20$ stars in the range $0.2 < (g - i)_0 < 1.5$, noted ZSL_0 . *Bottom panel:* Normalized histogram of the $(u_{\text{ISL}} - r)_0$ colour difference with respect to ZSL_0 for samples of different metallicities, defined with a central $[\text{Fe}/\text{H}] \pm 0.1$ dex. The central metallicity of each sample is labelled in the panel.

The median uncertainty in $[\text{Fe}/\text{H}]$ is 0.1 dex, providing a high-quality data set to derive the metallicity-dependent stellar locus.

Despite the large sky coverage of LAMOST, not all the J-PLUS pointings have metallicity information. We have 178 (16%) pointings with less than ten calibration stars in common with LAMOST. This implies that the metallicity-dependent stellar locus procedure detailed in Sect. 3.2.3 cannot be applied to all J-PLUS DR2 observations. We circumvented this limitation by modelling the offset in the stellar locus due to metallicity with MW location (Sect. 3.2.4).

3.2.2. Estimation of the metallicity-dependent stellar locus

The stellar locus is known to vary with metallicity (e.g. Yuan et al. 2015a). Such variation is more prominent at blue optical wavelengths, with the effect in the *u* band being an order of magnitude larger than in the *g* band (Yuan et al. 2015a). To illustrate this effect with J-PLUS photometry, the median $[\text{Fe}/\text{H}]$ from LAMOST in the $(u_{\text{ISL}} - r)_0$ versus $(g - i)_0$ colour-colour space is presented in the *top panel* of Fig. 2. At a given $(g - i)_0$ colour, redder stars in $(u_{\text{ISL}} - r)_0$ have larger metallicities.

As starting point, we defined the reference stellar locus, noted ZSL_0 , from those stars with $-0.25 < [\text{Fe}/\text{H}] < -0.20$ in the colour range $0.2 < (g - i)_0 < 1.5$. This metallicity range was chosen to cover the density peak in the distribution of LAMOST

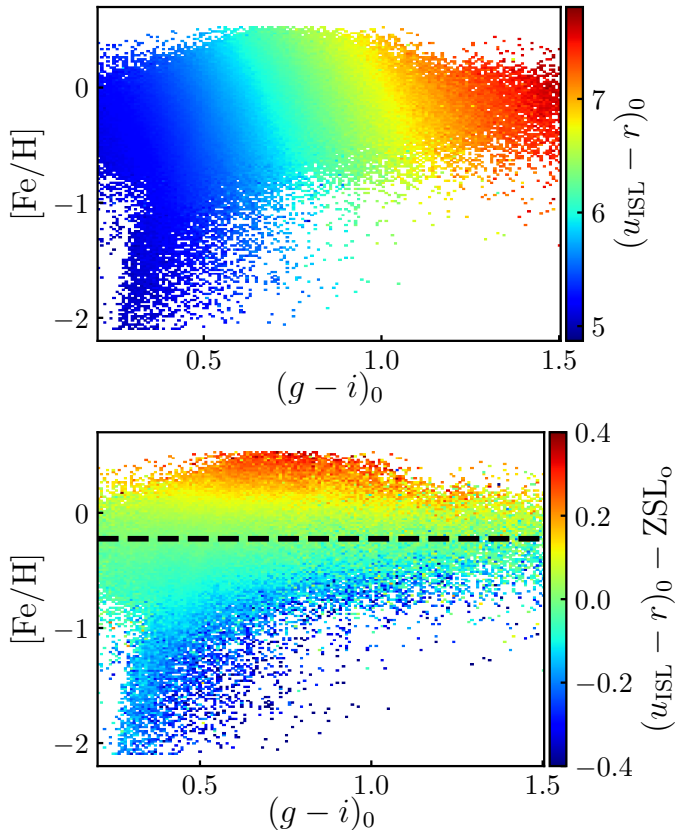


Fig. 3. Binned metallicity versus $(g - i)_0$ colour diagram of the MS calibration stars with measurements from LAMOST. *Top panel:* Mean $(u_{\text{ISL}} - r)_0$ colour in each bin, defining the metallicity-dependent stellar locus (ZSL). *Bottom panel:* $(u_{\text{ISL}} - r)_0$ colour difference with respect to ZSL_0 . The median metallicity of the reference locus is marked with the black dashed line.

metallicities. From the ZSL_0 reference, the colour difference for stars of different metallicities was computed, as shown in the *bottom panel* of Fig. 2. We find a $(u_{\text{ISL}} - r)_0$ colour difference of -0.20 mag for $[\text{Fe}/\text{H}] \sim -1.4$ dex stars, and of $+0.23$ mag for $[\text{Fe}/\text{H}] \sim 0.4$ dex stars. The dispersion with respect to the reference locus decreases by a factor of two from $\sigma = 0.092$ mag to $\sigma = 0.047$ mag after accounting for the metallicity dependence.

As shown by Yuan et al. (2015a), the metallicity-dependent stellar locus, noted ZSL, is not just a shift from the reference, and the simple modelling described above must be refined. Instead of performing an analytic fit to the data, we mapped the mean $(u_{\text{ISL}} - r)_0$ colour as a function of $[\text{Fe}/\text{H}]$ and $(g - i)_0$. The mapping was done with a two-dimensional histogram. The used ranges were $(g - i)_0 \in [0.2, 1.5]$ and $[\text{Fe}/\text{H}] \in [-2.1, 0.53]$, with 150 bins in each dimension. The effective bin width was 0.009 mag in colour and 0.017 dex in metallicity. The ZSL and its difference with respect to the reference locus ZSL_0 are shown in Fig. 3, highlighting the shift and the change in curvature of the stellar locus with metallicity. We compare the J-PLUS ZSL with the results from Yuan et al. (2015a) in Sect. 4.6.

3.2.3. Measurement of the metallicity offset

The ZSL estimated in the previous section can be used to compute the calibration offset due to metallicity in each J-PLUS DR2 pointing, named Δu_{FeH} . The star-by-star expected colour is esti-

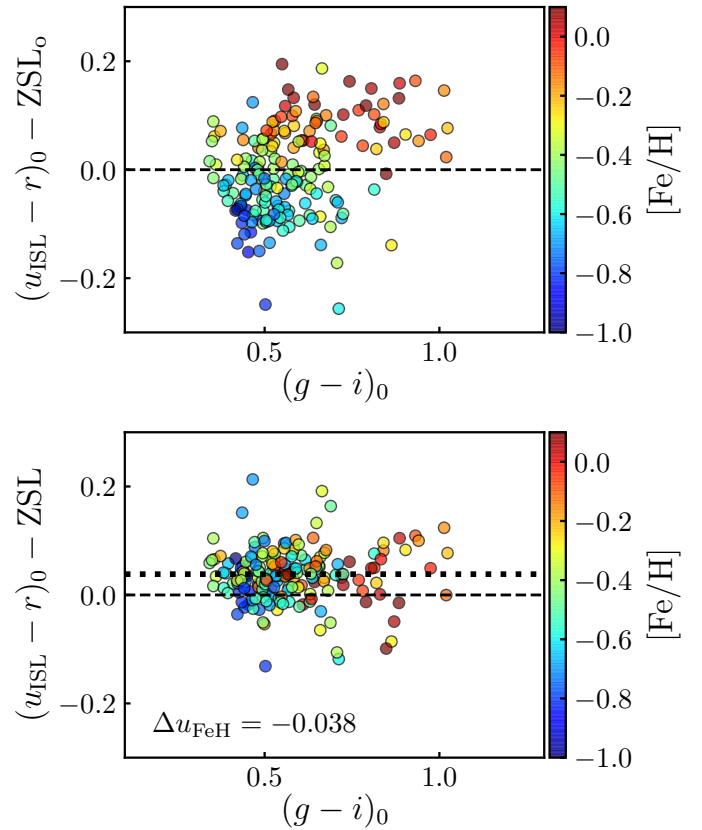


Fig. 4. $(u_{\text{ISL}} - r)_0$ colour difference with respect to the reference locus ZSL_0 (*top panel*) and the ZSL (*bottom panel*) as a function of $(g - i)_0$ for the MS calibration stars with LAMOST information in pointing $p_{\text{id}} = 00066$. The colored scale in both panels shows the spectroscopic $[\text{Fe}/\text{H}]$ from LAMOST. The dashed lines mark zero offset. The dotted line marks the median difference with respect to the ZSL. The derived metallicity offset is labelled in the *bottom panel*.

mated from the ZSL and subtracted to the observed colour,

$$\delta u_{\text{FeH}} = (u_{\text{ISL}} - r)_0 - \text{ZSL}. \quad (6)$$

The distribution of these differences in each pointing was fitted to a Gaussian with median $-\Delta u_{\text{FeH}}$, the targeted metallicity offset for the pointing. We assumed that the measured offset is due to the different metallicity, i.e. stellar locus location, of the stars in the pointing with respect to the J-PLUS ISL. In this process only ZSL bins with more than ten sources and pointings with more than 50 LAMOST stars with δu_{FeH} computed were kept.

We illustrate the process using the J-PLUS pointing $p_{\text{id}} = 00066$. The dispersion when no metallicity information is included is $\sigma = 0.09$ mag and a clear dependence with $[\text{Fe}/\text{H}]$ is present (*top panel* in Fig. 4). After accounting for metallicity effects with the ZSL, the dispersion reduces to $\sigma = 0.04$ and the $[\text{Fe}/\text{H}]$ gradient has disappeared (*bottom panel* in Fig. 4). The median of the measured δu_{FeH} is 0.038 mag, and the estimated metallicity offset is then $\Delta u_{\text{FeH}} = -0.038$ mag.

After applying the above procedure to all J-PLUS pointings, we obtained a valid Δu_{FeH} for 746 of them, 69% of the total targets. We study the trends in the derived offsets in the next section, and also detailed how we assigned a value to those orphan pointings without a measurement of the metallicity offset.

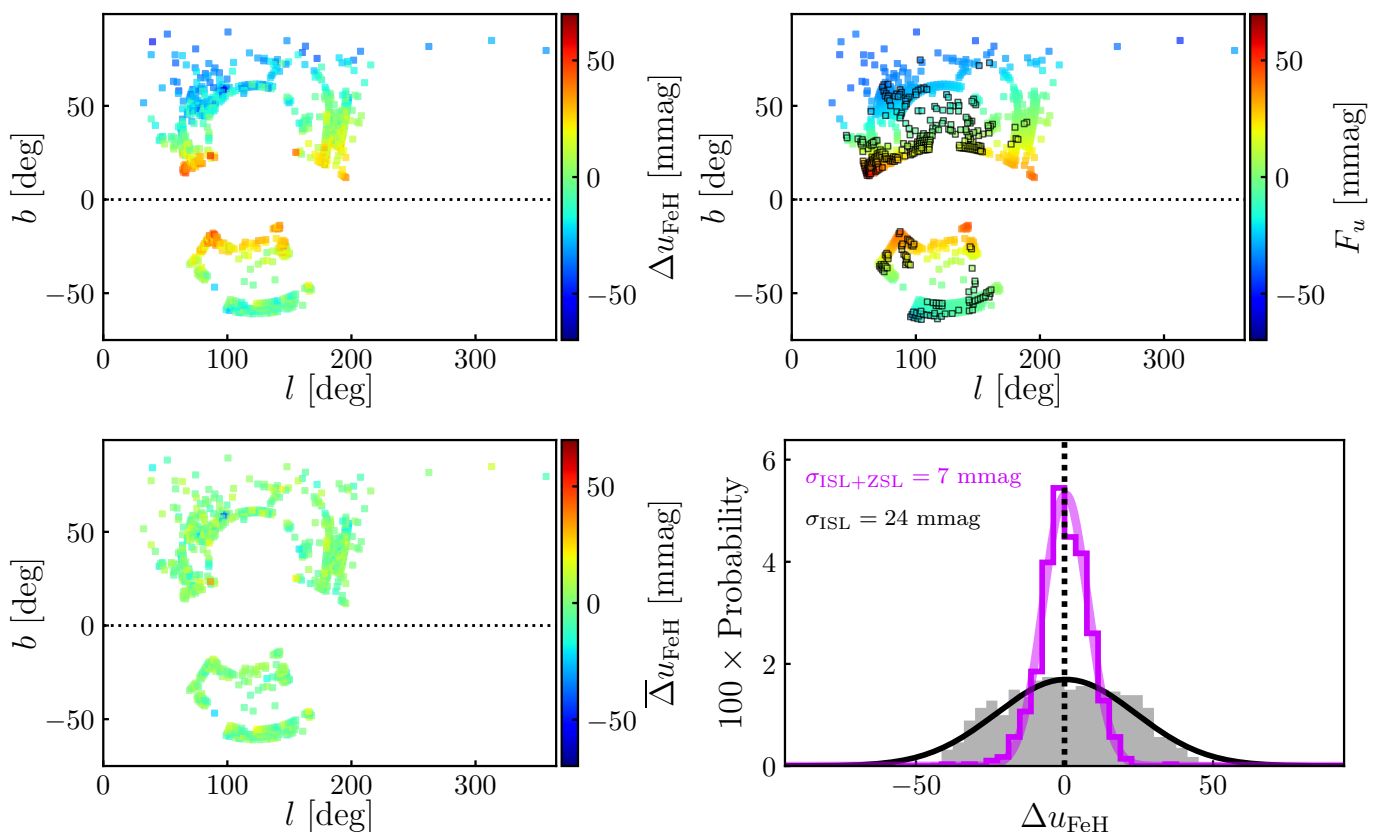


Fig. 5. Photometric offset for each J-PLUS DR2 pointing estimated from the metallicity-dependent stellar locus. *Top left panel:* Initial offset in galactic coordinates with the homogenization from ISL, Δu_{FeH} . *Top right panel:* Modelled metallicity offset F_u in galactic coordinates. Those pointings without offset estimation and not used in the modelling procedure are highlighted with a black edge. *Bottom left panel:* Final metallicity offset in galactic coordinates after the homogenization from ISL + ZSL, $\bar{\Delta}u_{\text{FeH}} = \Delta u_{\text{FeH}} - F_u$. *Bottom right panel:* Distribution of the metallicity offsets Δu_{FeH} (gray) and $\bar{\Delta}u_{\text{FeH}}$ (coloured). The Gaussian distributions that better describe the data are also shown, with their dispersion labelled in the panel. The dotted line marks zero offset.

3.2.4. Metallicity offset as a function of the pointing location and iterative process

The metallicity offsets for each J-PLUS pointing with a valid measurement are shown as a function of galactic coordinates in the *top left panel* of Fig. 5 (2D representation) and in the *top panels* of Fig. 6 (1D representation). We find a systematic trend in the offsets, changing from $\Delta u_{\text{FeH}} \sim +0.05$ mag to $\Delta u_{\text{FeH}} \sim -0.05$ mag as we move from low to high galactic latitudes. This trend mirrors the change in the metallicity of the pointings, computed as the median $[\text{Fe}/\text{H}]$ of the MS calibration stars with LAMOST information, noted $\langle [\text{Fe}/\text{H}] \rangle_{\text{LAMOST}}$, that changes from -0.1 dex to -0.5 dex (Fig. 6).

The dispersion in the distribution of the offsets is $\sigma_{\text{ISL}} = 24$ mmag (*bottom right panel* in Fig. 5), that translates to the observed edge-to-edge difference of ~ 0.1 mag. The key point of the estimated metallicity offsets is their systematic variation, that translates to a systematic shift in the calibration and poses a limitation to the scientific cases that depends on the information from the bluer J-PLUS passbands. As an example, we explore the impact in the estimation of photometric metallicity in Sect. 4.6.

To correct for the metallicity offsets, we modelled their variation with Galactic coordinates using a fourth degree polynomial fit,

$$F_u(l, b) = \sum_{m,n=0}^4 C_{mn} \times l^m \times b^n, \quad (7)$$

where (l, b) are the galactic longitude and latitude of the J-PLUS pointings, and C_{mn} are the coefficients of the polynomial. This modelling assumes a smooth variation of the metallicity, i.e. of the calibration offsets along the Galaxy. In addition, it permits to assign a metallicity offset to those orphan pointings without a valid measurement. As a drawback, local metallicity variations can still affect the calibration and in several cases the offsets are extrapolated from the area with available information.

The model F_u was applied as a proxy for the metallicity offset in Eq. (2). We note that this action changes the photometry of the J-PLUS stars used to compute the ZSL. To ensure self-consistency, we computed an updated version of the ZSL after obtaining the new calibration and iterate the process until convergence. It took four iterations to reach variations lower than 1 mmag in the measured metallicity offsets.

The final estimated model F_u for all the J-PLUS DR2 pointings is presented in the *top right panel* of Fig. 5. The final residuals, noted $\bar{\Delta}u_{\text{FeH}} = \Delta u_{\text{FeH}} - F_u$, have a dispersion of $\sigma_{\text{ISL+ZSL}} = 7$ mmag, three times smaller than the original ones (*bottom right panel* in Fig. 5). The improvement is also clear in the lower panels of Figs. 5 and 6, where the initial structures are suppressed and no systematic variations with the pointing location remain. This implies that the original systematic error is now statistical, greatly improving the accuracy of the J-PLUS calibration along the surveyed area (Sect. 4.2).

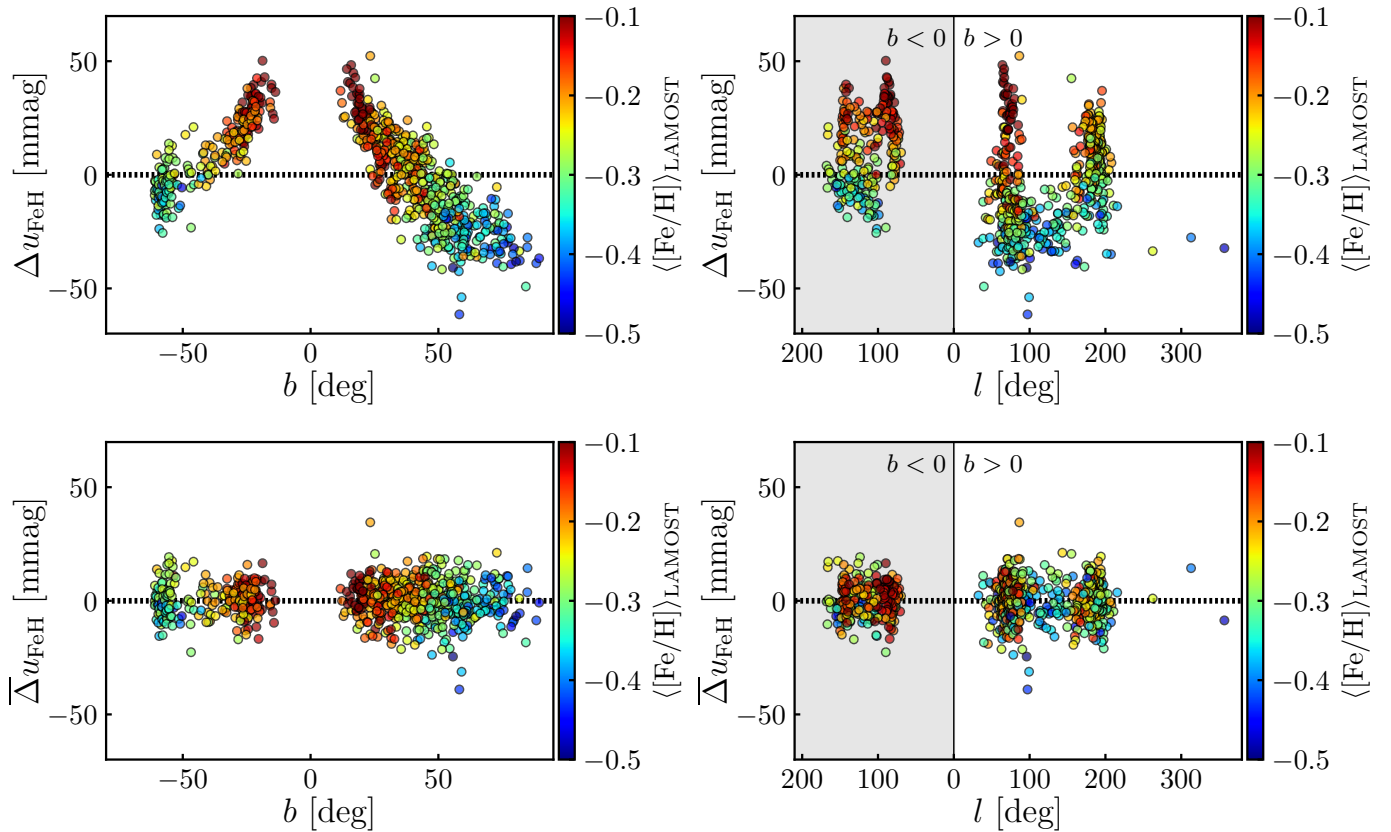


Fig. 6. Photometric offset estimated from the metallicity-dependent stellar locus. *Top panels:* Initial offset with the homogenization from ISL, Δu_{FeH} . *Bottom panels:* Final offset with the homogenization from ISL + ZS, $\bar{\Delta} u_{\text{FeH}} = \Delta u_{\text{FeH}} - F_u$. The *left panels* show the dependence on galactic latitude b and the *right panels* on galactic longitude l , showing pointings with positive and negative latitudes separately. In all the panels the colour scale shows the median metallicity in the pointing estimated from LAMOST spectra.

As a summary of this section, we have estimated and corrected the systematic impact of the varying MW metallicity in the stellar locus calibration. We have used the u passband as illustrative example, and the results for the other J-PLUS passbands are presented in Sect. 4.2.

4. Error budget and the impact of metallicity on photometric calibration

This section is devoted to the error budget analysis and the impact of the metallicity in the J-PLUS DR2 calibration. We study the precision in the photometry in Sect. 4.1, and the accuracy along the surveyed area in Sect. 4.2. The uncertainty in the absolute calibration is discussed in Sect. 4.3.

4.1. Precision from overlapping areas

J-PLUS pointings slightly overlap with each other. We measured the precision of the calibration by comparing the photometry of those MS calibration stars observed independently in the overlapping areas between adjacent pointings. We computed the differences in the calibrated magnitudes and estimated the median of the sources shared by every pair of overlapping pointings. We obtained 2 449 unique pair pointings in J-PLUS DR2. The distribution of these median differences was then used to estimate the precision in the calibration. The distributions are described by Gaussian functions and the desired precision is obtained as $\sigma/\sqrt{2}$, where σ is the measured dispersion.

We find that the precision obtained in $\chi_{\text{ISL+ZSL}}$ magnitudes is similar and replicates the results from J-PLUS DR1 at one mmag level. The results are summarised in Table 2. The measured precision is ~ 18 mmag in u , $J0378$, and $J0395$; ~ 9 mmag $J0410$ and $J0430$; and ~ 5 mmag in g , $J0515$, r , $J0660$, i , $J0861$, and z .

We also find that the results with χ_{ISL} magnitudes mimic those in Table 2. The negligible change with respect to DR1 and after applying the ZSL reflects that metallicity variations along the MW impacts the calibration at scales larger than a few square degrees. This limited local impact is exacerbated when distant pointings are compared, as analysed in the next section.

4.2. Accuracy along the surveyed area

The comparison of the photometry in adjacent pointings is not able to provide a measurement of the accuracy of the calibration along the surveyed area. This was a drawback of the analysis performed with J-PLUS DR1 by López-Sanjuan et al. (2019). As shown in Sect. 3.2.3, the systematic variation of the metallicity along the MW accordingly produces a systematic offset in the photometric solution. The metallicity offsets $\Delta\chi_{\text{FeH}}$ provides therefore a measurement of the accuracy in the calibration along the J-PLUS DR2 surveyed area (Fig. 7).

The dispersion in the metallicity offsets when χ_{ISL} magnitudes were used, noted $\sigma_{\text{ISL}}^{\text{acc}}$, are gathered in Table 2. However, the systematic nature of the offsets, with a clear smooth variation with galactic latitude (Fig. 6), implies that the relevant measure-

Table 2. Estimated error budget of the J-PLUS DR2 photometric calibration and final median zero points.

Passband	Precision			Accuracy				$\langle ZP_X \rangle$ [mag]
	$\sigma_{\text{ISL+ZSL}}^{\text{pre}}$ [mmag] ^a	σ_{WD} [mmag] ^b	σ_{cal} [mmag] ^c	$\sigma_{\text{ISL}}^{\text{acc}}$ [mmag] ^d	s_{ISL} [mmag] ^e	$\sigma_{\text{ISL+ZSL}}^{\text{acc}}$ [mmag] ^f	$\sigma_{\text{SCR}}^{\text{acc}}$ [mmag] ^g	
<i>u</i>	17	4	18	24	65	7	11	21.16
<i>J0378</i>	19	4	20	26	72	8	14	20.55
<i>J0395</i>	16	4	17	17	47	6	12	20.41
<i>J0410</i>	10	4	12	10	27	4	7	21.35
<i>J0430</i>	8	3	10	6	18	3	6	21.40
<i>g</i>	4	2	7	3	23.61
<i>J0515</i>	6	2	8	2	6	1	3	21.58
<i>r</i>	4	...	6	3	23.65
<i>J0660</i>	5	3	8	1	3	1	3	21.12
<i>i</i>	4	2	7	2	23.35
<i>J0861</i>	5	4	8	4	11	2	3	21.65
<i>z</i>	5	3	8	4	11	2	4	22.78

Notes. ^(a) Instrumental stellar locus (ISL), the plane correction to account for 2D variations along the CCD, and the metallicity-dependent stellar locus (ZSL) were used to homogenize the photometry. The calibration was anchored to PS1 photometry for *gri* passbands. Precision estimated from duplicated MS stars in overlapping pointings.

^(b) Uncertainty in the colour calibration from the Bayesian analysis of the white dwarf locus (Sect. 4.3).

^(c) Final precision in the J-PLUS DR2 flux calibration, $\sigma_{\text{cal}}^2 = \sigma_{\text{ISL+ZSL}}^2 + \sigma_{\text{WD}}^2 + \sigma_r^2$, where $\sigma_r = 5$ mmag (Sect. 4.3).

^(d) Dispersion in the metallicity offsets $\Delta\chi_{\text{FeH}}$ when the ISL was used to homogenize the photometry.

^(e) Accuracy along the surveyed area estimated from the difference between the percentile 95 and the percentile 5 in $\Delta\chi_{\text{FeH}}$ distribution when the ISL magnitudes were used.

^(f) Accuracy along the surveyed area estimated from the dispersion in $\Delta\chi_{\text{FeH}}$ when the ISL+ZSL were used to homogenize the photometry.

^(g) Accuracy estimated from the comparison of the final ISL+ZSL calibration with results from the Stellar Color Regression method (Sect. 4.5).

ment of the accuracy is not the dispersion, but the edge-to-edge ($\pm 2\sigma$) variation. In this context, we estimated the accuracy as the offset difference between the 5th percentile and the 95th percentile in $\Delta\chi_{\text{FeH}}$ distribution. This measurement is expressed as s_{ISL} in Table 2. We find that the calibration accuracy when metallicity effects are neglected is well above 1% for the passbands at $\lambda < 4500$ Å and accounts for $s_{\text{ISL}} \sim 0.07, 0.07, 0.05, 0.03$, and 0.02 mag in *u*, *J0378*, *J0395*, *J0410*, and *J0430*. The impact is milder in the redder passbands, with ~ 0.01 mag in *J0861* and *z*, and negligible in the *J0515* and *J0660* passbands.

The numbers above should be representative of the calibration accuracy of J-PLUS DR1, complementing the results presented in López-Sanjuan et al. (2019). The estimated systematic errors are much larger than the precision errors, limiting the J-PLUS scientific outcome when using the DR1 calibration. This is illustrated in Sect. 4.6.

The implementation of the metallicity-dependent stellar locus has greatly improved the accuracy in the J-PLUS calibration. It has not only decreased the dispersion in the final metallicity offsets by a factor of two-three (Fig. 7), but also removes the main systematic errors. This is, the dispersion is now a proper measurement of the accuracy in the calibration. The final uncertainty estimated for J-PLUS DR2 is summarised in Table 2 and it is at 1% level or below. The improvement in the bluer passbands is roughly a factor ten, decreasing from $s_{\text{ISL}} \sim 70 - 20$ mmag to $\sigma_{\text{ISL+ZSL}}^{\text{acc}} \sim 8 - 3$ mmag.

We conclude that the implementation of the metallicity-dependent stellar locus has improved the accuracy of the J-PLUS DR2 calibration to 1% level and has minimised the systematic in the photometric solution along the surveyed area.

4.3. Absolute colour calibration from the white dwarf locus

The stellar locus steps, both ISL and ZSL, are devoted to the homogenization of the J-PLUS photometry in those passbands not anchored to PS1. The absolute colour calibration was performed with the white dwarf locus. Thanks to the large area observed (2176 deg^2) and the already homogenized photometry, a set of 639 high-quality white dwarfs were retrieved from the *Gaia* absolute magnitude versus colour diagram. We performed a joint Bayesian analysis of the eleven $(\chi_{\text{ISL+ZSL}} - r)_0$ versus $(g - i)_0$ colour-colour diagrams to estimate the offsets $\Delta\chi_{\text{WD}}$ that translate instrumental magnitudes to calibrated magnitudes on top of the atmosphere. We summarise the obtained values in Table 3 for reference. The typical uncertainty in these offsets is at 4 mmag level, as presented also in Table 2.

In addition to the offsets, the Bayesian modeling provides the intrinsic dispersion in the WD locus (Table 3) and two physical parameters of the WD population, the fraction of DA and the median gravity. We find a DA fraction of $f_{\text{DA}} = 0.83 \pm 0.01$ and a median $\log g = 7.97 \pm 0.04$. Both values are consistent with J-PLUS DR1 results in López-Sanjuan et al. (2019) and the median surface gravity agrees with the literature (e.g. Jiménez-Esteban et al. 2018; Gentile Fusillo et al. 2019; Tremblay et al. 2019; Bergeron et al. 2019, and references therein). We refer the reader to López-Sanjuan et al. (2019) for a detailed description of the Bayesian modelling and the assumptions in the white dwarf locus step.

A relevant change with respect to J-PLUS DR1 is on the inferred offsets in the *g* and *i* passbands. We obtained $\Delta g_{\text{WD}} = 1$ mmag and $\Delta i_{\text{WD}} = -1$ mmag, while the values in DR1 were $\Delta g_{\text{WD}} = -3$ mmag and $\Delta i_{\text{WD}} = 4$ mmag, respectively. We attribute the better agreement between J-PLUS and PS1 photometric systems to the change in the colour excess and the extinction coefficients, as detailed in the next section.

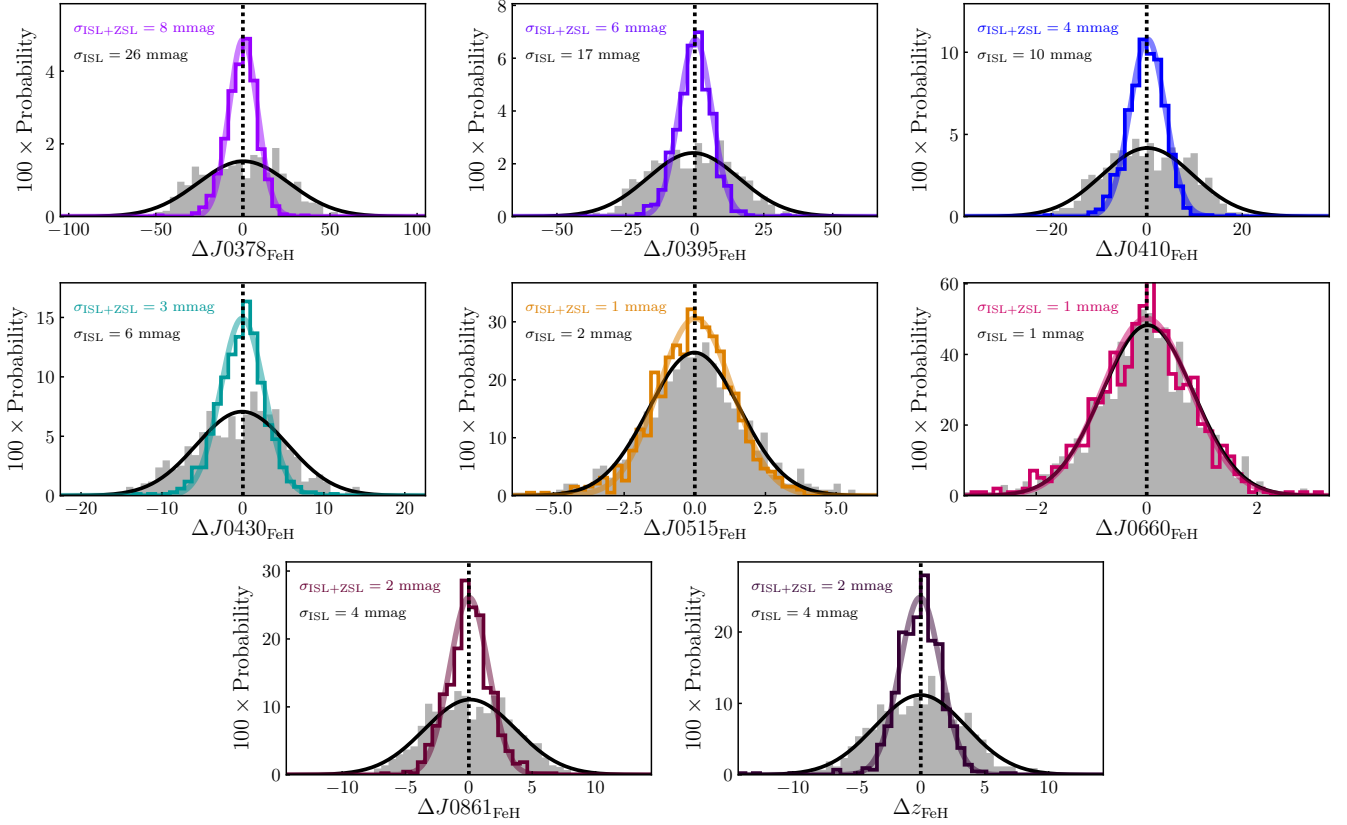


Fig. 7. Distribution of the metallicity offsets for J-PLUS DR2. In all the panels, the initial offsets ΔX_{FeH} from ISL magnitudes are presented in gray and the final offsets $\Delta \bar{X}_{\text{FeH}}$ computed with ISL+ZSL magnitudes in coloured. From top to bottom and left to right, passbands $J0378$, $J0395$, $J0410$, $J430$, $J0515$, $J0660$, $J0861$, and z are shown. The Gaussian distributions that better describe the data are also presented, with their dispersion labelled in each panel.

Table 3. Estimated offsets to transport the ISL+ZSL photometry outside the atmosphere, ΔX_{WD} , and intrinsic dispersion of the WD locus, σ_{int} . The r band was used as reference in the estimation of the colour offsets.

Passband (λ)	ΔX_{WD} [mag]	σ_{int} [mag]
u	-3.881 ± 0.004	0.030 ± 0.005
$J0378$	-4.497 ± 0.004	0.028 ± 0.005
$J0395$	-4.616 ± 0.004	0.028 ± 0.005
$J0410$	-3.662 ± 0.004	0.008 ± 0.005
$J0430$	-3.603 ± 0.003	0.007 ± 0.004
g	0.001 ± 0.002	0.004 ± 0.002
$J0515$	-3.438 ± 0.002	0.008 ± 0.003
r
$J0660$	-3.901 ± 0.003	0.019 ± 0.003
i	-0.001 ± 0.002	0.003 ± 0.002
$J0861$	-3.371 ± 0.004	0.013 ± 0.006
z	-2.250 ± 0.003	0.011 ± 0.004

Finally, we set the calibration uncertainty in the reference r band to $\sigma_r = 5$ mmag following the results in DR1. This uncertainty is added to the precision in the homogenization and the white dwarf locus offsets to provide the absolute flux uncertainty in J-PLUS DR2 (Table 2). The final precision is comparable to DR1 and the new calibration considerably improves the accuracy of our photometry.

4.4. Impact of the assumed colour excess in the calibration

We compared the final zero points obtained with the stellar and white dwarf loci against the zero points obtained by direct comparison with the PS1 z passband. The difference is well described by a Gaussian with median $\mu = -2$ mmag and a dispersion of $\sigma = 5$ mmag. This result reinforces the calibration procedure and was used to discriminate the best extinction model.

We repeated the full calibration process assuming the colour excess at infinity from Planck Collaboration et al. (2014) and with the 3D dust maps provided by Bayestar17⁴ (Green et al. 2018), based on Pan-STARRS stellar colours. We found that the best consistency with the PS1 z -band photometry is reached with the estimation based on Schlegel et al. (1998). In all the cases, the systematic offsets due to metallicity are present.

Interestingly, the application of the metallicity-dependent stellar locus to the X_{ISL} magnitudes worsen the comparison between J-PLUS and PS1 in the Bayestar17 case, going for $\sigma = 5$ mmag to $\sigma = 7$ mmag. The opposite happened in the Planck and Schlegel et al. (1998) cases, improving from $\sigma = 6$ mmag to $\sigma = 5$ mmag. The differences are subtle, but measurable. We suggest that the Bayestar17 extinction, derived from the variation of the PS1 stellar locus, is containing part of the colour variation due to metallicity. The extinction maps from Schlegel et al. (1998) and Planck Collaboration et al. (2014) are not related with the photometry used in the calibration, providing therefore an independent frame for the homogenization process.

⁴ <http://argonaut.skymaps.info/>

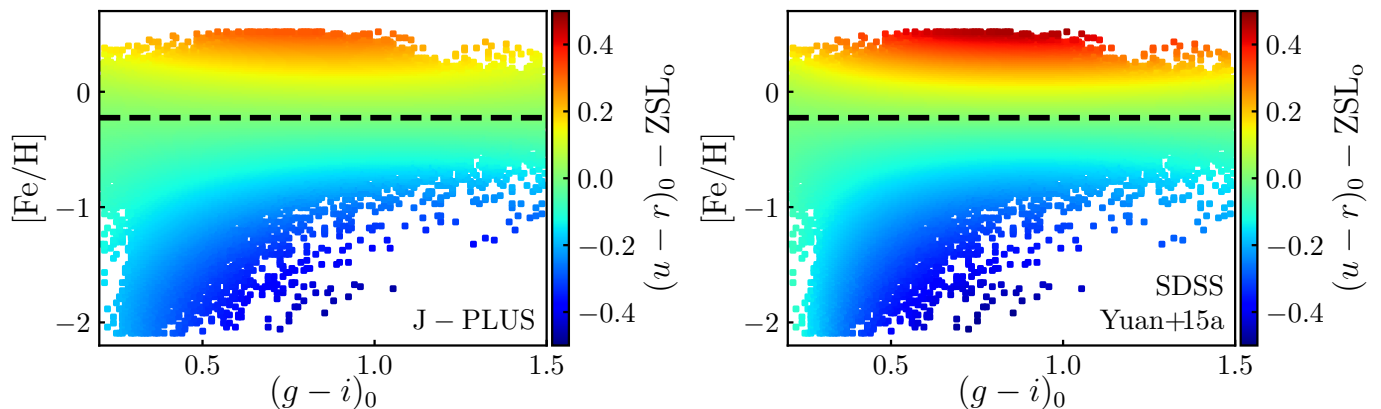


Fig. 8. Modelled $(u-r)_0$ colour difference with respect to the reference locus, ZSL_0 , as a function of $(g-i)_0$ and $[Fe/H]$. The median metallicity of the reference locus is marked with the black dashed line. *Left panel:* Estimation from J-PLUS DR2 final photometry. *Right panel:* Estimation from Yuan et al. (2015a) using SDSS photometry.

4.5. Comparison with the SCR method

As already pointed out in Sect. 1, the stellar color regression (SCR; Yuan et al. 2015b; Huang et al. 2020) method deals with the different stellar properties in a consistent way, providing an alternative homogenization process for the calibration. Using LAMOST DR5 as reference, the SCR method has been applied to J-PLUS DR2.

We found that the comparison between the ISL+ZSL and the SCR zero points follows a Gaussian distribution with dispersion σ_{SCR}^{acc} , as summarised in Table 2. The dispersion is ~ 12 mmag in the u , $J0378$, and $J0395$ filters, ~ 6 mmag in $J0410$ and $J0430$, and ~ 3 mmag in the rest of the J-PLUS passbands. The origin of this dispersion is related with the different treatment of the interstellar extinction, our functional approach to the impact of the metallicity offset, and the inherent statistical dispersion of each method.

A detailed application and analysis of the SCR calibration for J-PLUS DR2 is beyond the scope of the present paper and will be presented in a forthcoming work. The comparison with the independent SCR method provided an extra measurement for the accuracy in the photometry, that we set at percent level for passbands bluer than $\lambda \sim 4500$ Å.

4.6. Photometric metallicity from J-PLUS data

In this section, we highlight the impact of the improved calibration in the estimation of the photometric metallicity from J-PLUS DR2 data. As in other sections, we use the u band as example, but similar results are obtained with J-PLUS passbands $J0378$ and $J0395$, which are the most sensitive to metallicity.

We started by computing the final ZSL in the $(u-r)_0$ versus $(g-i)_0$ space as in Sect. 3.2, but using the final J-PLUS DR2 calibrated magnitudes. Following Yuan et al. (2015a), we modelled the $(u-r)_0$ locus with a fourth degree polynomial in $(g-i)_0$ and $[Fe/H]$. The resulting model in those bins with data was normalized to the expected locus at $[Fe/H] = -0.225$ dex, as shown in the *left panel* of Fig. 8. The curvature in the locus is evident.

We compared the J-PLUS ZSL with the results from Yuan et al. (2015a) using SDSS photometry. They provide the metallicity-dependent stellar locus $(u-g)_0$ and $(g-r)_0$ as a function of $(g-i)_0$ and $[Fe/H]$. We combined both loci to obtain the $(u-r)_0$ variation and normalized again to the expected locus at $[Fe/H] = -0.225$ dex. The result is presented in the *right panel*

of Fig. 8. We find a close agreement between both studies, that obtain similar structures and general variations for the ZSL. The discrepancies, at 0.04 mag level, are expected because of the different photometric systems used (J-PLUS versus SDSS).

After checking our final ZSL with the results in Yuan et al. (2015a), we aim to test the impact of the calibration in the photometric metallicities estimated from J-PLUS DR2. We decided to compute the J-PLUS photometric metallicities using the simplest offset model, relating the $(u-r)_0$ colour distance to the reference locus at $[Fe/H] = -0.225$ dex with a $[Fe/H]$ measurement. We used 144 375 stars in common with LAMOST and with $0.1 \leq (g-i)_0 \leq 1.6$ to map the relation between colour and metallicity. The comparison between J-PLUS and LAMOST metallicities has a dispersion of $\sigma = 0.14$ dex. We stress that the goal of this section is just to illustrate the net improvement of the photometric calibration. We expect to get better metallicity estimates from the whole twelve-band J-PLUS photometry (e.g. Whitten et al. 2019).

Because LAMOST metallicities were used in both the calibration and the estimation of the photometric metallicity, we ensured an independent test by comparing J-PLUS metallicities with the spectroscopic values from the Apache Point Observatory Galactic Evolution Experiment (APOGEE, Jönsson et al. 2020) latest data release (SDSS DR16⁵). The available data contains high-resolution ($R \sim 22500$), near-infrared (15 140 – 16 940 Å) spectra for about 430 000 stars covering both the Northern and Southern sky, from which radial velocities, stellar parameters, and chemical abundances of 20 species are determined.

We cross-matched the MS calibration stars with the APOGEE sample using 1 arcsec radius. A total flag equal to zero in APOGEE information and a J-PLUS colour $0.1 \leq (g-i)_0 \leq 1.6$ was imposed. This yields 2 177 common stars. The difference between the J-PLUS and APOGEE values was defined as

$$\Delta[Fe/H] = [Fe/H]_{J-PLUS} - [Fe/H]_{APOGEE}. \quad (8)$$

The star-by-star difference defines a Gaussian with median $\mu = 0.03$ dex and dispersion $\sigma = 0.13$ dex.

To explore the possible systematic trend of $\Delta[Fe/H]$ with galactic latitude, we computed the median metallicity difference with respect to APOGEE using 25 bins of variable size to ensure ~ 90 sources per bin. The uncertainties were estimated by

⁵ https://www.sdss.org/dr16/irspec/dr_synopsis/

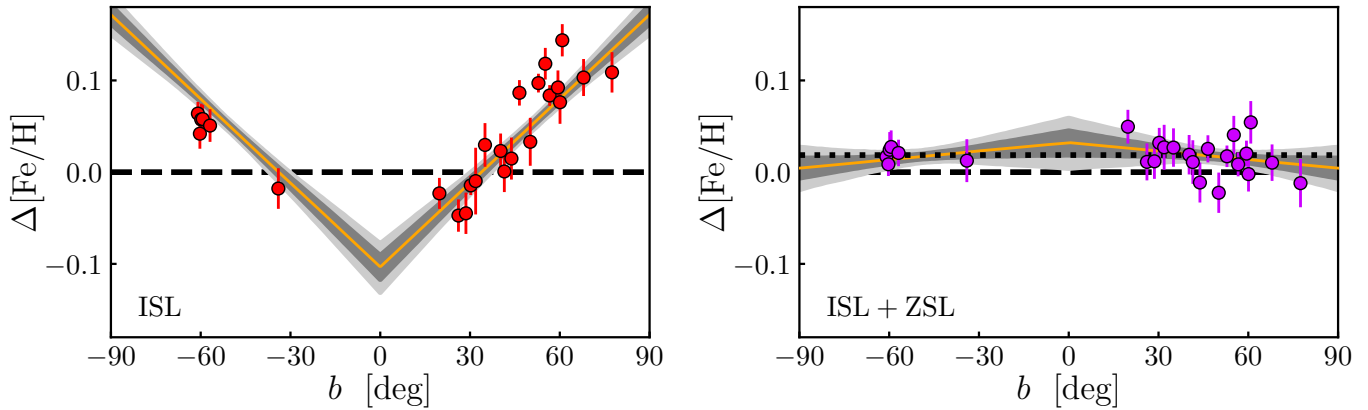


Fig. 9. Metallicity difference between J-PLUS photometric values and APOGEE spectroscopic values, $\Delta[\text{Fe}/\text{H}]$, as a function of galactic latitude b . *Left panel:* Using χ_{ISL} photometry. *Right panel:* Using $\chi_{\text{ISL+ZSL}}$ photometry. The solid line in both panels shows the best linear fitting to the data, with the gray areas depicting the 68% and 95% confidence intervals. The dashed lines marks zero difference. The dotted line in the *right panel* shows a difference of 0.02 dex.

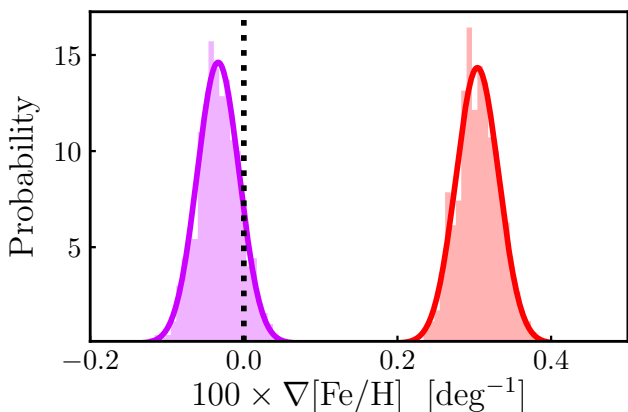


Fig. 10. Distribution in the best linear-fitting slope of the metallicity difference versus galactic latitude estimated from χ_{ISL} (red) and $\chi_{\text{ISL+ZSL}}$ (purple) photometry. The dotted line marks a zero slope.

bootstrapping. The results using χ_{ISL} magnitudes and the final calibration are presented in Fig. 9. We found that the metallicity differences are roughly flat with the final J-PLUS DR2 calibration, as desired, presenting a slight bias of 0.02 dex. However, neglecting the ZSL step in the calibration produces a clear trend with galactic latitude: the estimated $\Delta[\text{Fe}/\text{H}]$ changes from -0.02 dex at $|b| \sim 30$ deg to $+0.10$ dex at $|b| \sim 80$ deg. We performed a linear fit to the data, using $|b|$ as independent variable, and present the distribution of the slope $\nabla[\text{Fe}/\text{H}]$, with $[\text{deg}^{-1}]$ units, in Fig. 10. The slope for the final calibration is $100 \times \nabla[\text{Fe}/\text{H}] = -0.03 \pm 0.03$, while neglecting the ZSL step provides $100 \times \nabla[\text{Fe}/\text{H}] = 0.3 \pm 0.03$. The slope is compatible with zero, as desired, by including the impact of metallicity in the stellar locus position, while the slope is positive at 10σ level when the metallicity effects are not accounted for.

We conclude that the improved photometric calibration of J-PLUS DR2 yields a reliable twelve-bands photometric catalog for an important fraction of the Northern sky.

5. Summary and conclusions

We have explored the impact of metallicity on the photometric calibration of J-PLUS DR2, based on the stellar locus technique, and update the error budget in the calibration.

Using the metallicity information from LAMOST, we find that the J-PLUS passbands bluer than 4500 \AA are strongly affected by the Milky Way metallicity gradient in Galactic latitude, that breaks the assumption of an homogeneous dust de-reddened stellar locus across the sky. The peak-to-peak variation amounts 0.07, 0.07, 0.05, 0.03, and 0.02 mag in u , $J0378$, $J0395$, $J0410$, and $J0430$, respectively. The variation is of ~ 0.01 mag in $J0861$ and z , while negligible in $J0515$ and $J0660$. This effect is systematic and smooth along the surveyed area. We modelled the metallicity-dependent offset in the stellar locus in those areas in common with LAMOST to improve the photometric calibration in the complete J-PLUS DR2 data set. The accuracy of the calibration in the surveyed area is expected to be at percent level for the bluer J-PLUS passbands and sub-percent in the rest of the filters after including the metallicity information in the process.

The precision in the calibration, measured from repeated sources in the overlapping areas between pointings and including absolute colour and flux scale uncertainties, is ~ 18 mmag in u , $J0378$, and $J0395$; ~ 11 mmag in $J0410$ and $J0430$; and ~ 8 mmag in g , $J0515$, r , $J0660$, i , $J0861$, and z . These values are similar to those derived in López-Sanjuan et al. (2019) with J-PLUS DR1 data, reflecting that the metallicity impacts the calibration at scales larger than a few square degrees.

Our analysis highlights the expected impact of metallicity on the stellar locus technique at $\lambda \lesssim 4500 \text{ \AA}$ (see High et al. 2009; Yuan et al. 2015a), producing systematic offsets at a few degree scale and impacting the physical properties derived for stars and galaxies. Large-area surveys with blue optical passbands must evaluate the impact of metallicity in the use of the stellar locus to homogenize their photometry, and techniques based on large overlapping areas or methods that accounts for the variety of stars' physical properties (e.g., SCR or ISL+ZSL) should be favoured.

Regarding the technical goal of J-PLUS, i.e. ensure the photometric calibration of J-PAS, the lessons learnt have been of great importance to define the J-PAS calibration strategy. The current roadmap for J-PAS calibration has three steps: (1) homogenization using half-CCD overlapping areas thanks to a large dithering pattern between the four exposures per filter. This will permit to derive a consistent photometric solution along the surveyed area by comparing four measurements of the same source, and to trace 2D variations along the focal plane. (2) Absolute colour calibration using the white dwarf locus. The prop-

erties of the locus, with two populations and curved profiles, will permit the colour calibration without using external photometric data. (3) Absolute calibration by anchoring the J-PAS reference broad-band to Pan-STARRS. In this case only one offset will be needed to translate the already homogeneous photometry outside the atmosphere. The calibration against *Gaia* is also a possibility, but with J-PAS photometry being independent of *Gaia* spectro-photometry it will be possible to test systematic effects in both surveys.

Acknowledgements. We dedicate this paper to the memory of our six IAC colleagues and friends who met with a fatal accident in Piedra de los Cochinos, Tenerife, in February 2007, with special thanks to Maurizio Panniello, whose teachings of python were so important for this paper. We thank the relevant discussions and suggestions from the J-PLUS collaboration members. Based on observations made with the JAST/T80 telescope at the Observatorio Astrofísico de Javalambre (OAJ), in Teruel, owned, managed, and operated by the Centro de Estudios de Física del Cosmos de Aragón. We acknowledge the OAJ Data Processing and Archiving Unit (UPAD) for reducing the OAJ data used in this work. Funding for the J-PLUS Project has been provided by the Governments of Spain and Aragón through the Fondo de Inversiones de Teruel; the Aragón Government through the Reseach Groups E96, E103, and E16_17R; the Spanish Ministry of Science, Innovation and Universities (MCIU/AEI/FEDER, UE) with grants PGC2018-097585-B-C21 and PGC2018-097585-B-C22; the Spanish Ministry of Economy and Competitiveness (MINECO) under AYA2015-66211-C2-1-P, AYA2015-66211-C2-2, AYA2012-30789, and ICTS-2009-14; and European FEDER funding (FCDD10-4E-867, FCDD13-4E-2685). The Brazilian agencies FINEP, FAPESP, and the National Observatory of Brazil have also contributed to this project. E. J. A. acknowledges financial support from PGC2018-095049-B-C21 (MCIU/AEI/FEDER, UE) and SEV-2017-0709. A. A. C. acknowledges support from the Universidad de Alicante (contract UATALENTO18-02). The work of V. M. P. is supported by NOIRLab, which is managed by the Association of Universities for Research in Astronomy (AURA) under a cooperative agreement with the National Science Foundation. E. T. acknowledges support by ETAG grant PRG1006 and by EU through the ERDF CoE grant TK133. L. S. J. acknowledges support from Brazilian agencies FAPESP (2019/10923-5) and CNPq (304819/201794). Guoshoujing Telescope (the Large Sky Area Multi-Object Fiber Spectroscopic Telescope LAMOST) is a National Major Scientific Project built by the Chinese Academy of Sciences. Funding for the project has been provided by the National Development and Reform Commission. LAMOST is operated and managed by the National Astronomical Observatories, Chinese Academy of Sciences. The Pan-STARRS1 Surveys (PS1) and the PS1 public science archive have been made possible through contributions by the Institute for Astronomy, the University of Hawaii, the Pan-STARRS Project Office, the Max-Planck Society and its participating institutes, the Max Planck Institute for Astronomy, Heidelberg, and the Max Planck Institute for Extraterrestrial Physics, Garching, The Johns Hopkins University, Durham University, the University of Edinburgh, the Queen's University Belfast, the Harvard-Smithsonian Center for Astrophysics, the Las Cumbres Observatory Global Telescope Network Incorporated, the National Central University of Taiwan, the Space Telescope Science Institute, the National Aeronautics and Space Administration under Grant No. NNX08AR22G issued through the Planetary Science Division of the NASA Science Mission Directorate, the National Science Foundation Grant No. AST-1238877, the University of Maryland, Eotvos Lorand University (ELTE), the Los Alamos National Laboratory, and the Gordon and Betty Moore Foundation. This work has made use of data from the European Space Agency (ESA) mission *Gaia* (<https://www.cosmos.esa.int/gaia>), processed by the *Gaia* Data Processing and Analysis Consortium (DPAC, <https://www.cosmos.esa.int/web/gaia/dpac/consortium>). Funding for the DPAC has been provided by national institutions, in particular the institutions participating in the *Gaia* Multilateral Agreement. Funding for SDSS-III has been provided by the Alfred P. Sloan Foundation, the Participating Institutions, the National Science Foundation, and the U.S. Department of Energy Office of Science. The SDSS-III web site is <http://www.sdss3.org/>. SDSS-III is managed by the Astrophysical Research Consortium for the Participating Institutions of the SDSS-III Collaboration including the University of Arizona, the Brazilian Participation Group, Brookhaven National Laboratory, Carnegie Mellon University, University of Florida, the French Participation Group, the German Participation Group, Harvard University, the Instituto de Astrofísica de Canarias, the Michigan State/Notre Dame/JINA Participation Group, Johns Hopkins University, Lawrence Berkeley National Laboratory, Max Planck Institute for Astrophysics, Max Planck Institute for Extraterrestrial Physics, New Mexico State University, New York University, Ohio State University, Pennsylvania State University, University of Portsmouth, Princeton University, the Spanish Participation Group, University of Tokyo, University of Utah, Vanderbilt University, University of Virginia, University of Washington, and Yale University. Funding for the Sloan Digital Sky Survey IV has been provided by the Alfred

P. Sloan Foundation, the U.S. Department of Energy Office of Science, and the Participating Institutions. SDSS-IV acknowledges support and resources from the Center for High Performance Computing at the University of Utah. The SDSS website is www.sdss.org. SDSS-IV is managed by the Astrophysical Research Consortium for the Participating Institutions of the SDSS Collaboration including the Brazilian Participation Group, the Carnegie Institution for Science, Carnegie Mellon University, Center for Astrophysics | Harvard & Smithsonian, the Chilean Participation Group, the French Participation Group, Instituto de Astrofísica de Canarias, The Johns Hopkins University, Kavli Institute for the Physics and Mathematics of the Universe (IPMU) / University of Tokyo, the Korean Participation Group, Lawrence Berkeley National Laboratory, Leibniz Institut für Astrophysik Potsdam (AIP), Max-Planck-Institut für Astronomie (MPIA Heidelberg), Max-Planck-Institut für Astrophysik (MPA Garching), Max-Planck-Institut für Extraterrestrische Physik (MPE), National Astronomical Observatories of China, New Mexico State University, New York University, University of Notre Dame, Observatório Nacional / MCTI, The Ohio State University, Pennsylvania State University, Shanghai Astronomical Observatory, United Kingdom Participation Group, Universidad Nacional Autónoma de México, University of Arizona, University of Colorado Boulder, University of Oxford, University of Portsmouth, University of Utah, University of Virginia, University of Washington, University of Wisconsin, Vanderbilt University, and Yale University. This research made use of *Astropy*, a community-developed core Python package for Astronomy (Astropy Collaboration et al. 2013), and *Matplotlib*, a 2D graphics package used for Python for publication-quality image generation across user interfaces and operating systems (Hunter 2007).

References

- Aihara, H., Allende Prieto, C., An, D., et al. 2011, *ApJS*, 193, 29
- Astropy Collaboration, Robitaille, T. P., Tollerud, E. J., et al. 2013, *A&A*, 558, A33
- Benítez, N., Dupke, R., Moles, M., et al. 2014, [ArXiv:1403.5237]
- Bergeron, P., Dufour, P., Fontaine, G., et al. 2019, *ApJ*, 876, 67
- Bertin, E. & Arnouts, S. 1996, *A&AS*, 117, 393
- Bonoli, S., Marín-Franch, A., Varela, J., et al. 2020, *A&A*, submitted [arXiv:2007.01910]
- Cenarro, A. J., Moles, M., Cristóbal-Hornillos, D., et al. 2019, *A&A*, 622, A176
- Cenarro, A. J., Moles, M., Marín-Franch, A., et al. 2014, in *Proc. SPIE*, Vol. 9149, *Observatory Operations: Strategies, Processes, and Systems V*, 91491I
- Chambers, K. C., Magnier, E. A., Metcalfe, N., et al. 2016, [arXiv:1612.05560]
- Covey, K. R., Ivezić, Ž., Schlegel, D., et al. 2007, *AJ*, 134, 2398
- Cui, X.-Q., Zhao, Y.-H., Chu, Y.-Q., et al. 2012, *Research in Astronomy and Astrophysics*, 12, 1197
- Cukanovaite, E., Tremblay, P. E., Freytag, B., Ludwig, H. G., & Bergeron, P. 2018, *MNRAS*, 481, 1522
- Deng, L.-C., Newberg, H. J., Liu, C., et al. 2012, *Research in Astronomy and Astrophysics*, 12, 735
- Flewelling, H. A., Magnier, E. A., Chambers, K. C., et al. 2016, [arXiv:1612.05243]
- Gaia* Collaboration, Brown, A. G. A., Vallenari, A., et al. 2018, *A&A*, 616, A1
- Gaia* Collaboration, Prusti, T., de Bruijne, J. H. J., et al. 2016, *A&A*, 595, A1
- Gentile Fusillo, N. P., Tremblay, P.-E., Gänsicke, B. T., et al. 2019, *MNRAS*, 482, 4570
- Green, G. M., Schlafly, E. F., Finkbeiner, D., et al. 2018, *MNRAS*, 478, 651
- High, F. W., Stubbs, C. W., Rest, A., Stalder, B., & Challis, P. 2009, *AJ*, 138, 110
- Huang, Y., Yuan, H., Li, C., et al. 2020, *ApJ*, in press [arXiv:2011.07172]
- Hunter, J. D. 2007, *Computing In Science & Engineering*, 9, 90
- Ivezić, Ž., Sesar, B., Jurić, M., et al. 2008, *ApJ*, 684, 287
- Jiménez-Esteban, F. M., Torres, S., Rebassa-Mansergas, A., et al. 2018, *MNRAS*, 480, 4505
- Jönsson, H., Holtzman, J. A., Prieto, C. A., et al. 2020, *AJ*, 160, 120
- Kelly, P. L., von der Linden, A., Applegate, D. E., et al. 2014, *MNRAS*, 439, 28
- Kesseli, A. Y., West, A. A., Veyette, M., et al. 2017, *ApJS*, 230, 16
- Kuijken, K., Heymans, C., Dvornik, A., et al. 2019, *A&A*, 625, A2
- Lenz, D. D., Newberg, J., Rosner, R., Richards, G. T., & Stoughton, C. 1998, *ApJS*, 119, 121
- Li, L., Shen, S., Hou, J., et al. 2018, *ApJ*, 858, 75
- López-Sanjuan, C., Varela, J., Cristóbal-Hornillos, D., et al. 2019, *A&A*, 631, A119
- Luo, A. L., Zhao, Y.-H., Zhao, G., et al. 2015, *Research in Astronomy and Astrophysics*, 15, 1095
- Magnier, E. A., Chambers, K. C., Flewelling, H. A., et al. 2016a, [arXiv:1612.05240]
- Magnier, E. A., Schlafly, E. F., Finkbeiner, D. P., et al. 2016b, [arXiv:1612.05242]

Magnier, E. A., Sweeney, W. E., Chambers, K. C., et al. 2016c, [arXiv:1612.05244]
Marín-Franch, A., Taylor, K., Cenarro, J., Cristobal-Hornillos, D., & Moles, M. 2015, in IAU General Assembly, Vol. 29, 2257381
Oke, J. B. & Gunn, J. E. 1983, ApJ, 266, 713
Planck Collaboration, Abergel, A., Ade, P. A. R., et al. 2014, A&A, 571, A11
Schlegel, D. J., Finkbeiner, D. P., & Davis, M. 1998, ApJ, 500, 525
Starkenburger, E., Martin, N., Youakim, K., et al. 2017, MNRAS, 471, 2587
Tonry, J. L., Stubbs, C. W., Lykke, K. R., et al. 2012, ApJ, 750, 99
Tremblay, P. E., Cukanovaite, E., Gentile Fusillo, N. P., Cunningham, T., & Hollands, M. A. 2019, MNRAS, 482, 5222
Tremblay, P. E., Ludwig, H. G., Steffen, M., & Freytag, B. 2013, A&A, 559, A104
Varela, J. & J-PLUS collaboration. 2021, in preparation
Waters, C. Z., Magnier, E. A., Price, P. A., et al. 2016, [arXiv:1612.05245]
Whitten, D. D., Placco, V. M., Beers, T. C., et al. 2019, A&A, 622, A182
Wu, Y., Luo, A. L., Li, H.-N., et al. 2011, Research in Astronomy and Astrophysics, 11, 924
Yuan, H., Liu, X., Xiang, M., Huang, Y., & Chen, B. 2015a, ApJ, 799, 134
Yuan, H., Liu, X., Xiang, M., et al. 2015b, ApJ, 799, 133
Yuan, H. B., Liu, X. W., Huo, Z. Y., et al. 2015c, MNRAS, 448, 855
Yuan, H. B., Liu, X. W., & Xiang, M. S. 2013, MNRAS, 430, 2188
Zhao, G., Zhao, Y.-H., Chu, Y.-Q., Jing, Y.-P., & Deng, L.-C. 2012, Research in Astronomy and Astrophysics, 12, 723